Search for axion dark matter with the QUAX–LNF tunable haloscope

A. Rettaroli,[1,*] D. Alesini,[1] D. Babusci,[1] C. Braggio,[2,3] G. Carugno,[2] D. D'Agostino,[4,5] A. D'Elia,[1] D. Di Gioacchino,[1] R. Di Vora,[6] P. Falferi,[7,8] U. Gambardella,[4,5] A. Gardikiotis,[2] C. Gatti,[1] C. Ligi,[1] A. Lombardi,[6] G. Maccarrone,[1] A. Ortolan,[6] G. Ruoso,[6] S. Tocci,[1,†] and G. Vidali[9,1]

(QUAX Collaboration)

[1]*INFN, Laboratori Nazionali di Frascati, Frascati, Roma, Italy*
[2]*INFN, Sezione di Padova, Padova, Italy*
[3]*Dipartimento di Fisica e Astronomia, Padova, Italy*
[4]*Dipartimento di Fisica E.R. Caianiello, Fisciano, Salerno, Italy*
[5]*INFN, Sezione di Napoli, Napoli, Italy*
[6]*INFN, Laboratori Nazionali di Legnaro, Legnaro, Padova, Italy*
[7]*Istituto di Fotonica e Nanotecnologie, CNR Fondazione Bruno Kessler, I-38123 Povo, Trento, Italy*
[8]*INFN, TIFPA, Povo, Trento, Italy*
[9]*Dipartimento di Fisica, Università La Sapienza, Rome, Italy*

(Received 25 March 2024; accepted 24 June 2024; published 23 July 2024)

We report the first experimental results obtained with the new haloscope of the QUAX experiment located at Laboratori Nazionali di Frascati of INFN (LNF). The haloscope is composed of a OFHC Cu resonant cavity cooled down to about 30 mK and immersed in a magnetic field of 8 T. The cavity frequency was varied in a 6 MHz range between 8.831496 and 8.83803 GHz. This corresponds to a previously unprobed mass range between 36.52413 and 36.5511 μeV. We don't observe any excess in the power spectrum and set limits on the axion-photon coupling in this mass range down to $g_{a\gamma\gamma} < 0.882 \times 10^{-13}$ GeV^{-1} with the confidence level set to 90%.

DOI: 10.1103/PhysRevD.110.022008

I. INTRODUCTION

In recent years, we witnessed an increasing growth in the research of light dark matter (DM) candidates, addressing in particular axions and axionlike particles (ALPs). If axions are found to exist, they would untie the long-standing DM problem [1,2], after being originally postulated as a solution to the strong *CP* problem [3,4]. The nature of a pseudoscalar, electrically neutral, and feebly interacting particle makes the axion a strong DM candidate [5–7], and its cosmological evolution and astrophysical constraints indicate a favorable mass range between $1\ \mu\text{eV} < m_a < 10$ meV [8].

The research efforts are now spread over many different detection approaches, but the paradigm has become the haloscope design proposed by Sikivie [9,10], which probes axions from the DM halo of the Galaxy. Currently operating haloscopes are ADMX [11–14], HAYSTAC [15–17], ORGAN [18,19], CAPP-8T [20,21], CAPP-9T [22], CAPP-PACE [23], CAPP-18T [24], CAST-CAPP [25], CAPP-12TB [26], GrAHal [27], RADES [28–30], TASEH [31], and QUAX [32–38], whereas among the proposed experiments are FLASH [39], BabyIAXO/RADES [40], ABRACADABRA [41], DM-Radio [42,43], CADEx [44], MADMAX [45], ALPHA [46], WISPLC [47], DALI [48], BRASS [49], BREAD [50], and SUPAX [51].

The axion observation technique is based upon its inverse Primakoff conversion into one photon, stimulated by a static magnetic field. The essential elements required to run a haloscope are a superconducting magnet to generate a strong magnetic field, a microwave resonant cavity where the electromagnetic field excitation builds up, an ultralow noise receiver, a tuning mechanism to scan over the axion mass range, and a cryogenic system to grant operation at low temperature. The two figures of merit in the axion search are the power of the produced photon [52]

$$P_{a\gamma} = \left(\frac{g_{a\gamma\gamma}^2}{m_a^2}\hbar^3 c^3 \rho_a\right)\left(\frac{\beta}{1+\beta}\omega_c \frac{1}{\mu_0} B_0^2 V C_{010} Q_L\right) \times \left(\frac{1}{1+(2Q_L \Delta\omega_c/\omega_c)^2}\right), \quad (1)$$

and the scan rate [53]

*Contact author: alessio.rettaroli@lnf.infn.it
†Contact author: simone.tocci@lnf.infn.it

$$\frac{\mathrm{d}f}{\mathrm{d}t} = g_{a\gamma\gamma}^4 \frac{\rho_a^2}{m_a^2} \frac{1}{\mathrm{SNR}^2} \left(\frac{B_0^2 V C_{010}}{k_B T_{\mathrm{sys}}}\right)^2 \times \frac{\beta^2}{(1+\beta)^2} Q_a \min(Q_L, Q_a). \quad (2)$$

We assume a local DM density $\rho_a = 0.45$ GeV/cm^3 [54], m_a is the axion mass, and $g_{a\gamma\gamma}$ is its coupling constant to photons. B_0 is the applied magnetic field; $\omega_c = 2\pi\nu_c$, V, Q_L, β are, respectively, the resonance angular frequency of the cavity, the volume, the loaded quality factor, and the antenna coupling to the cavity. The relation $Q_L = Q_0/(1+\beta)$ holds, with Q_0 the intrinsic quality factor. C_{010} is a mode-dependent geometrical factor, about 0.69 for the TM010 resonant mode of a cylindrical cavity, and $\Delta\omega_c = \omega_c - \omega_a$ is the detuning between the cavity and the axion angular frequency defined as $\omega_a = m_a c^2/\hbar$. The quality factor $Q_a \approx 10^6$ [55] is related to the energy spread in the cold dark matter halo. In Eq. (2), the signal-to-noise ratio, SNR, is defined as the ratio between the signal power and the uncertainty of the noise power, $\mathrm{SNR} \equiv P_{a\gamma}/\delta P_{\mathrm{noise}}$, while T_{sys} is the system noise temperature, whose reduction is of fundamental importance in speeding up the scan rate of the experiment.

In this paper, we report on the first operation of the new QUAX haloscope located at the National Laboratories of Frascati (LNF), which doubles the search potential of the QUAX experiment along with the LNL haloscope [38]. The experiment is conducted using a resonant cavity equipped with a tuning rod mechanism allowing one to exclude the existence of dark matter axions with coupling $g_{a\gamma\gamma}$ down to 0.882×10^{-13} GeV^{-1} in the mass window (36.5241–36.5510) μeV.

II. EXPERIMENTAL SETUP

A. Haloscope description

The haloscope, schematized in Fig. 1, consists of a cylindrical OFHC copper resonant cavity, with inner radius $r = 13.51$ mm and height $h = 246$ mm, for a total volume $V = 0.141$ l. The body is divided into two semicylinders, including the endcaps, sealed together with screws. Two coaxial cables are coupled to the cavity via dipole antennas. One antenna is fixed and weakly coupled, with coupling estimated from simulations 1.4×10^{-3}, and verified to be less than 7×10^{-3} from calibration data, such that Eqs. (1) and (2) are still valid. The other is obtained by stripping the end of a coax cable, leaving only the central conductor for a 2 mm length (bottom left panel of Fig. 2). The coax cable is connected to a linear stepper motor whose movement allows the tunability of the coupling β.

The magnetic field is provided by a NbTi superconducting solenoid magnet with a cold bore diameter of 100 mm and 320 mm height. On top of the magnet, a second coil assures the reduction of the stray field above the cavity

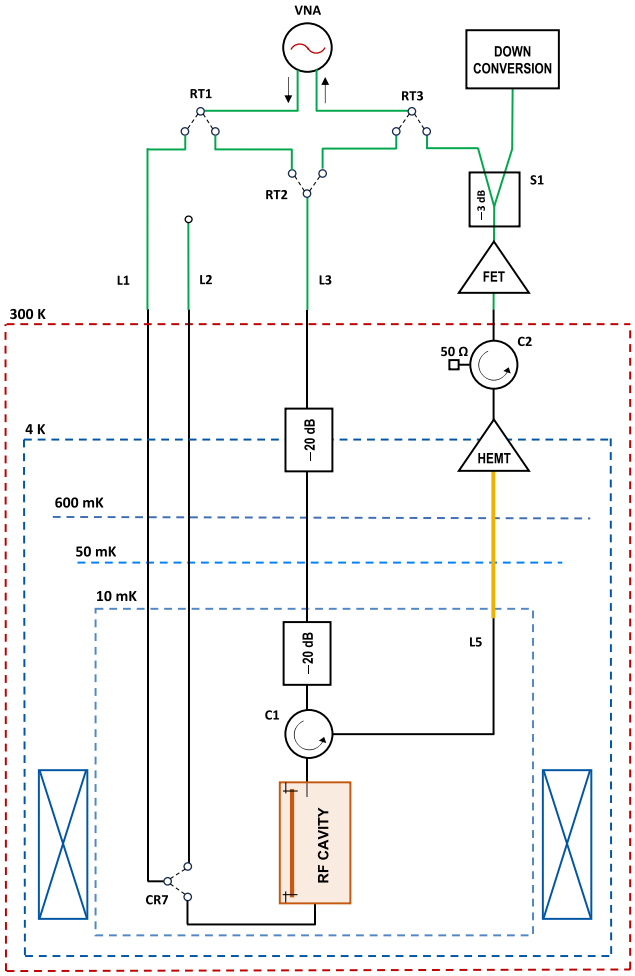

FIG. 1. Experimental setup sketch. The successive temperature stages of the dilution refrigerator are shown with their base temperature. $L1$ and $L3$ are input rf lines, $L5$ is the output amplified line, and $L2$ is an auxiliary line used for further checks. Note that $L1$, $L2$, and $L3$ have intrinsic attenuations of about 15 dB each. The room temperature switches (RT1, RT2, RT3), and the cryogenic switch (CR7) allow all the combinations required for measurements and calibrations. Attenuators are indicated with their attenuation values, while $C1$ and $C2$ are circulators. A superconductive rf cable in $L5$ is indicated in yellow. The magnet is shown as two crossed squares and is thermalized in the 4 K vessel. The HEMT and FET are, respectively, the cryogenic and room-temperature amplifiers, whereas the power splitter is indicated as $S1$.

below few hundred Gauss. The magnet, initially operated at the nominal field of 9 T, was set to a lower safety value following a quench during a current ramp. The experiment here described was then conducted at 8 T, with a field inside the cavity volume of r.m.s. $\sqrt{\langle B_0^2 \rangle} = 6.73$ T.

The power collected through the tunable antenna is amplified along the output line $L5$ (see Fig. 1) by the first amplification stage consisting in a cryogenic high electron mobility transistor (HEMT) amplifier. The circulator $C1$ allows the routing of the rf signals and provides the

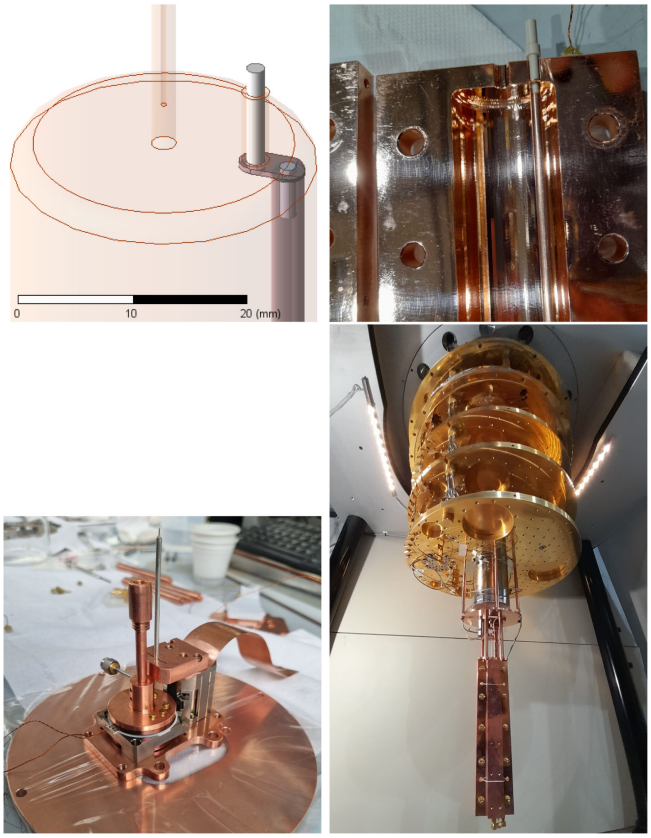

FIG. 2. Experimental setup closeups. Upper left: Detail of the rod tuning mechanism design as seen in the simulator. Upper right: Picture of one end of the rod with the PEEK support, placed in one of the two cavity halves. Bottom left: Stepper motors detail. On the left is the rotative motor together with the mandrel to cling the rod support, and on the right is the linear motor holding the movable antenna. Bottom right: View of the assembled haloscope, with the resonant cavity attached to the 20 mK stage with copper bars.

isolation of the cavity from the HEMT. The HEMT output signal reaches a room temperature field-effect (FET) amplifier through a second circulator, $C2$, and is then split and transmitted to the downconversion electronics or to a Vector Network Analyzer (VNA) by means of the switch $S1$.

The setup is hosted in a Leiden Cryogenics CF-CS110-1000 dilution refrigerator equipped with two Sumitomo pulse tubes with cooling power of 1.5 W at 4 K each. The refrigerator is segmented into different temperature stages. The magnet and the HEMT are thermalized at the 4 K stage, while the cavity is connected to the last temperature stage, which attained 20 mK at equilibrium. The cavity temperature, monitored during the data taking, reached about 30 mK.

B. Tuning mechanism

The frequency tuning is obtained by moving a copper rod with radius 1.5 mm and length 244 mm inside the cavity volume (Fig. 2). The effective cavity volume is then reduced to $V = 0.139$ l. The rod is supported by PEEK nails, which are centered off axis with respect to the rod, as shown in Fig. 2. At one end, the PEEK is grabbed by a copper mandrel, which is rotated by the stepper motor. Thanks to this movement, the rod accomplishes an arc of circumference approaching the center of the cavity. The electromagnetic behavior of this system was simulated with the ANSYS HFSS suite [56]. The resonant mode of interest, TM010, has a starting frequency of 8.817 GHz when the (ideal) rod is at rest in contact with the cavity wall. Moving the rod toward the center, the mode is squeezed, and simulations indicate that the frequency is tuned up to 9.106 GHz with a rotation of 80 degrees, while keeping the geometric factor C_{010} close to its ideal value and with a reduction of the quality factor of about 10%.

The rod orientation is changed by a rotative stepper piezoelectric motor from Attocube Systems model ANR240, while the second linear motor, as anticipated, moves the tunable antenna (model ANPz111). Both motors were operated at cryogenic temperatures, between 20 and 30 mK, without complications, and with a heating up of the environment of only a few mK when operated in single-step mode.

Although the intrinsic quality factor of the cavity without the tuner is measured to be $Q_0 \simeq 10^5$ at cryogenic temperatures, the PEEK supporting the rod and nonideality of the

TABLE I. Cavity resonance frequency, quality factor, and cavity-antenna coupling for each dataset of the scan.

ν_c [GHz]	Q_L	β
8.83176900	32 345	0.5206
8.83203080	32 228	0.519
8.83229550	32 273	0.5082
8.83255580	32 332	0.5141
8.83282190	32 387	0.5097
8.83307310	32 401	0.5078
8.83334500	32 300	0.5097
8.83360070	32 503	0.5058
8.83386200	32 540	0.5075
8.83412790	32 752	0.5014
8.83438580	32 573	0.5026
8.83464620	32 904	0.5005
8.83490660	32 957	0.4984
8.83516350	32 863	0.4951
8.83542850	32 872	0.4947
8.83568970	33 326	0.4881
8.83594630	33 051	0.489
8.83620570	33 056	0.4894
8.83646975	33 104	0.4857
8.83672330	33 584	0.4823
8.83698660	33 529	0.4803
8.83724500	33 659	0.4823
8.83750860	33 639	0.4793
8.83776640	33 450	0.4793

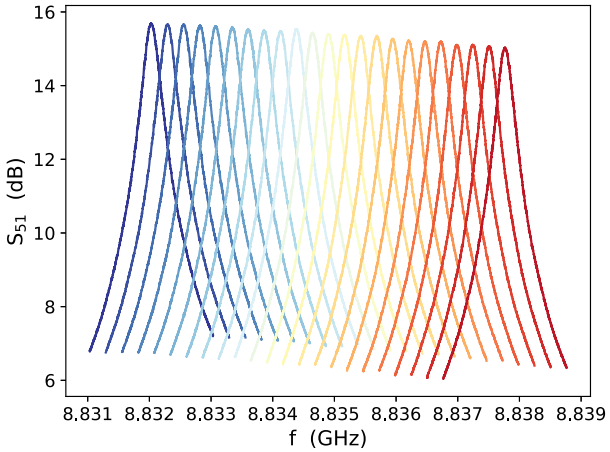

FIG. 3. Transmission spectra (S_{51}) of the haloscope cavity for different resonant frequencies. We tuned the resonance of the cavity in the 6 MHz frequency window during the axion search.

rod itself caused field losses, reducing the quality factor to about 50 000 (Sec. II C). The coupling, supposed to be equal to the optimal value for scan $\beta = 2$, resulted to be $\beta = 0.5$ after a more accurate analysis of calibration data. The values of Q_L and β measured before the data taking at different frequencies are listed in Table I, while the transmission spectra measured with the VNA are shown in Fig. 3.

C. Data taking

After the cooldown, the following procedure is used for calibrating and taking data at each frequency step, starting from the first measured value of 8.8317690 GHz.

(i) The cavity frequency is set moving the ANR240 motor step by step while monitoring the S_{51} from the VNA. Each time, the frequency is increased by one cavity bandwidth, about 260 kHz, with respect to the previous data taking.

(ii) The waveforms of the scattering parameters S_{51}, S_{53}, and S_{13}, named according to the line numbering in Fig. 1, are collected with the VNA, to perform the calibration.

(iii) The raw data acquisition is started, lasting about 3600 s.

The data acquisition consists in recording the power coming from the output line $L5$. During data acquisition, the switch CR7 is closed on line $L2$ to avoid noise leakage through the under coupled port, the switch RT1 is closed on the line L1, and the switch RT2 is closed on the switch RT3 which, in turn, is closed on a 50 ohm termination (not shown in Fig. 1). Finally, the splitter $S1$ allows one to redirect the signal to the downconversion and acquisition electronics. Here, with an I–Q mixer, we convert the frequency to the baseband, and the I and Q quadratures are amplified by low-noise voltage amplifiers ($\times 10^3$ factor, 10 MHz bandwidth) before being digitized by a 16-bit ADC board, which has a 2 MHz bandwidth and sampling of 2 MS/s. In each subrun, the I and Q signals are acquired for 4 seconds and saved to a file. The total amount of files in each subrun is 941, resulting in an integration time of $\Delta t = 3764$ s.

The calibration procedure (refer to Appendix A 2 for more details) is done by a simultaneous fit of the S_{51}, S_{53}, and S_{13} spectra with their analytical expressions, allowing the extraction of the cavity parameters ν_c, Q_0, β, and of the attenuation and gain of the input and output lines (see Fig. 4). In particular, we are interested in the gain of Line 5, which is calculated solving a system of three coupled equations [Eq. (A2)]. The measured gain through all the subruns is

$$G_{L5} = (70.62 \pm 0.28_{\text{syst}} \pm 0.13_{\text{stat}})\ \text{dB}, \tag{3}$$

where the systematic uncertainty is mainly due to the gain flatness of the reconstracted G_{L5}, and the statistic uncertainty derives from the data scattering of the S_{13} trace. This gain is referred at the input of the splitter, having subtracted the cable contributions from the splitter to the VNA and the −3 dB of the splitter itself. Then, the gain spectrum from the splitter output to the ADC is measured, taking into account the effect of the ADC internal filters.

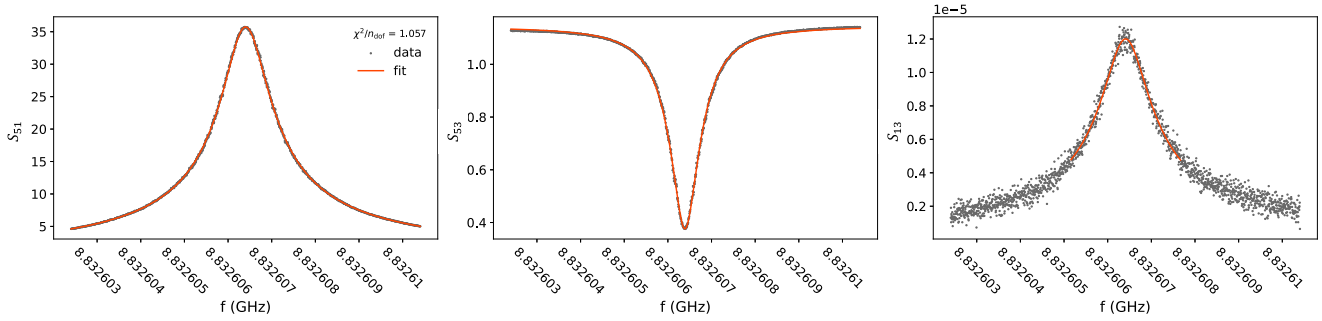

FIG. 4. Fit example of the scattering parameters S_{51} (forward transmission), S_{53} (reflection), and S_{13} (backward transmission) to extract the cavity parameters and gain in the calibration.

III. DATA ANALYSIS AND RESULTS

The cavity resonance frequency ν_c is tuned in a 6 MHz range between 8.831769–8.8377664 GHz in 24 steps. The parameters of each of the 24 datasets are reported in Table I. For each dataset, we calculate the power spectrum by combining the quadratures as $I - iQ$, computing the FFT and taking the squared module. The spectra are centered at the LO frequency, which is always $\nu_{\rm LO} = \nu_c - 500$ kHz, and are corrected for the Line 5 gain G_5 and for the spectrum shape of the downconversion electronics.

For each frequency step, we estimate $T_{\rm sys}$ from the output power, properly converted into units of Kelvin, at a reference frequency $\nu_{\rm LO} + 100$ kHz, where 1/f noise is negligible and still far enough from the cavity resonance, obtaining an average value of 4.7 K. Across the dataset, we observe that the power spectra line shapes show features typical of Fano interference, as recently reported in [57] where similar interference phenomena in microwaves measurements were analyzed. We interpret the bump structure as due to a imperfect isolation and thermalization of the circulator, attenuators, and the rod inside the cavity, leading to effective temperatures greater than expected from thermalization; in particular, we estimate $T_{\rm circ} \approx 450$ mK and $T_{\rm cav} \approx 100$ mK (see Appendix A 3 for further details). This effect does not affect the extraction of the power generated by axion conversion since it adds incoherently.

In the presence of axion conversions, a power surplus is expected in the cavity power spectrum as given by Eq. (1). We calculate the power spectrum residuals by subtracting it from a polynomial obtained with a Savitzky-Golay (SG) filter [58] from the spectrum itself. We adopt a SG filter of the fourth order with a dynamic interval of 250.5 kHz (501 bins). We apply the SG filter in a window $[\nu_c - \Gamma, \nu_c + \Gamma]$ of about 530 kHz for each dataset. Γ is the cavity linewidth and is calculated as ν_c/Q_L. An example of polynomial obtained from a SG filter from one of the datasets is shown in Fig. 5. The slope in the power spectrum is due to aliasing of the thermal noise at the edge of the Nyquist window, while the bump structure is due to the imperfect thermalization and isolation of the rf components connected to the resonant cavity, as pointed out earlier. We normalize the residuals to the expected noise power $\sigma_{\rm Dicke}$ for each dataset, where $\sigma_{\rm Dicke}$ is calculated using the Dicke radiometer equation [59]

$$\sigma_{\rm Dicke} = k_B T_{\rm sys} \sqrt{\Delta\nu/\Delta t}, \tag{4}$$

where $T_{\rm sys}$, is the system noise temperature, $\Delta\nu$ is the bin width (500 Hz), and Δt is the integration time (3764 s). The distribution of the normalized residuals obtained combining all the datasets is shown in Fig. 6. The data follow a Gaussian distribution, with a standard deviation compatible with 1.

For each axion mass, we apply the least-squares method to estimate the best value $\hat{g}_{a\gamma\gamma}$ by minimizing

$$\chi^2 = \sum_{\alpha=1}^{N_{\rm scan}} \sum_{i=1}^{N_{\rm bin}} \left[\frac{R_{\alpha,i} - S_{\alpha,i}(m_a, g^2_{a\gamma\gamma})}{\sigma^{(\alpha)}_{\rm Dicke}} \right]^2, \tag{5}$$

where the α index runs over the number of datasets ($N_{\rm scan}$), and the index i runs over the frequency bins of each power spectrum. $S_{\alpha,i}$ and $R_{\alpha,i}$ are the expected power signal and the residuals for frequency bin i and the dataset α. We calculate $S_{\alpha,i}$ as the integral in the frequency domain of Eq. (1) multiplied by the spectrum of the full standard halo model distribution [55].

Expressing $S_{\alpha,i}(m_a, g^2_{a\gamma\gamma}) = g^2_{a\gamma\gamma} T_{\alpha,i}(m_a)$, we analytically minimize Eq. (5) by solving $\partial\chi^2/\partial g^2_{a\gamma\gamma} = 0$ and calculate the uncertainty according to the formula ($\xi = g^2_{a\gamma\gamma}$):

$$\frac{1}{\sigma^2_{\hat{\xi}}} = \frac{1}{2}\frac{\partial^2\chi^2}{\partial^2\xi}. \tag{6}$$

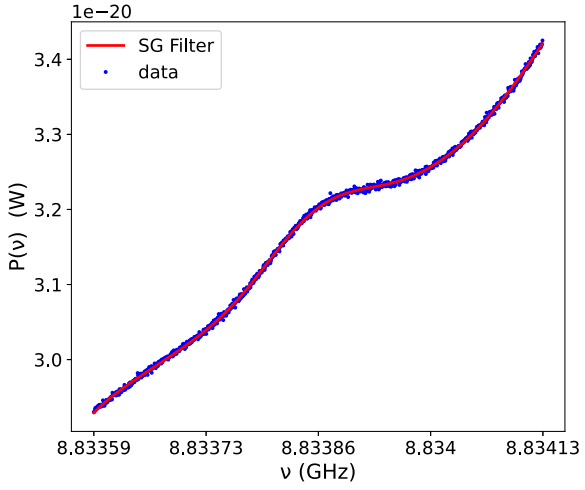

FIG. 5. FFT cavity power spectrum (blue dots) and SG filter (red line). $\nu_c = 8.833862$ GHz, $Q_L = 32540$.

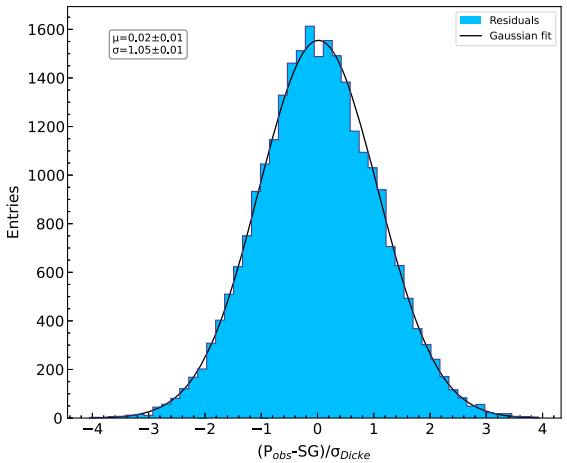

FIG. 6. Distribution of the cumulative residuals normalized to $\sigma_{\rm Dicke}$.

Minimizing Eq. (5), we find: ($\sum\sum \equiv \sum_{\alpha=1}^{N_{\rm scan}} \sum_{i=1}^{N_{\rm bin}}$)

$$\overline{g^2} = \sigma^2(\overline{g^2})\left[\sum\sum \frac{R_{\alpha,i}T_{\alpha,i}(m_a)}{(\sigma_{\rm Dicke}^{(\alpha)})^2}\right], \tag{7}$$

where $\overline{g^2}$ is the average squared coupling constant that incorporates the contributions of all the frequency bins from all the datasets, and

$$\sigma^2(\overline{g^2}) = \sum\sum\left[\frac{T_{\alpha,i}(m_a)}{\sigma_{\rm Dicke}^{(\alpha)}}\right]^2 \tag{8}$$

is its variance. We repeat this procedure for different values of m_a in the range 36.5241–36.5510 μeV. The detection of a power excess larger than 5σ above the noise is required for a candidate discovery. Since no candidates are found (Fig. 6), we determine the exclusion limits for $g_{a\gamma\gamma}$ in this mass range as follows.

To correctly estimate these limits, we account for the efficiency of the filtering procedure used for the extraction of the axion signal. We follow the procedure reported in [37]. We run a Monte Carlo simulation numerically injecting a fake axion signal, with a known $g^2_{\rm injected}$, into simulated power spectra with different ν_c. We use Eq. (7) to estimate the $g^2_{\rm injected}$ for each injected signal (i.e., obtaining $g^2_{\rm calculated}$). Hence, we determine the efficiency from the relation between $g^2_{\rm calculated}$ and $g^2_{\rm injected}$. To simulate the cavity power spectra, we add random Gaussian noise (with mean = 0, sigma = $\sigma_{\rm Dicke}$, according to a Gaussian PDF) to the SG filters. Applying this procedure, we estimate a detection efficiency of 0.845 on $g^2_{\rm calculated}$ for the SG filter. After correcting for the estimated efficiency, we calculate the single-sided upper limit on the axion-photon coupling with a 90% confidence level as in [36]. We use a power constrained procedure for the $\overline{g^2}$ that under fluctuates below $-\sigma$ [60]. In Fig. 7, we show the upper-limit $g^{\rm CL}_{a\gamma\gamma}$ in an axion mass window of 27.02 neV centered around 36.53764 μeV. The maximum sensitivity obtained with a 90% CL is $g^{\rm CL}_{a\gamma\gamma} < 0.882 \times 10^{-13}$ GeV^{-1}. This value is about six times larger with respect to the benchmark QCD axion level of the KSVZ theory [61,62].

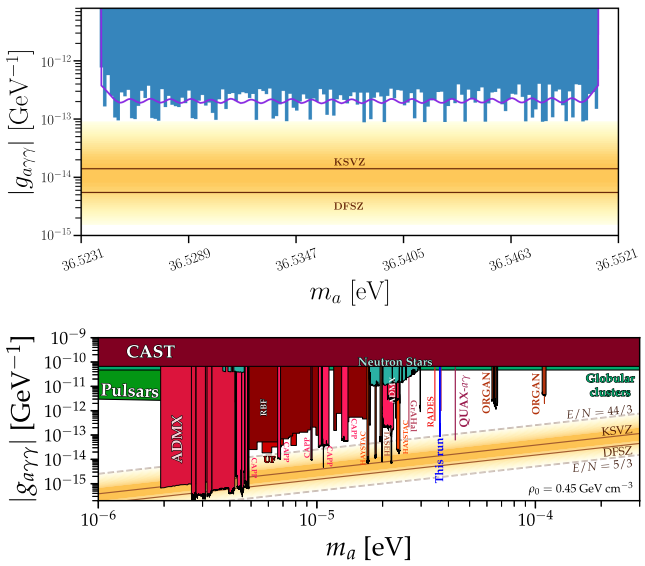

FIG. 7. Top: The 90% single-sided CL upper limit for $g_{a\gamma\gamma}$ as a function of the axion mass. The violet solid curve represents the expected limit in the case of no signal. The yellow region indicates the QCD axion model band. Bottom: Broad view of axion exclusion limits set by haloscopes. The blue vertical line indicates the search presented in this paper. Images realized with [63].

IV. CONCLUSIONS

In this paper, we described the first search for axion dark matter with the tunable QUAX–LNF haloscope. The operation of a microwave cavity resonating at 8.8 GHz and equipped with a movable tuning rod in a magnetic field of 8 T, placed in a stable ultra-cryogenic environment, demonstrated to be successful. Taking data with this setup for a total amount of about 25 hours through 6 MHz allowed us to exclude the existence of axion dark matter in a mass range between 36.52413 and 36.5511 μeV with axion-photon coupling $g_{a\gamma\gamma}$ down to 0.882×10^{-13} GeV^{-1} with a CL of 90%.

The apparatus still has much room for improvement. In the upcoming future, the sensitivity can be boosted employing a superconducting resonant cavity, enhancing the intrinsic quality factor. Adding a Josephson Parametric Amplifier as a preamplification stage, the importance of which has been widely demonstrated in this field, will break the noise temperature down by 1 order of magnitude. Moreover, the rod design can be optimized: (i) reducing the amount of dielectric exposed to the electromagnetic mode of the cavity, (ii) placing the lower end of the bar directly in contact with the end cap of the cavity eliminating PEEK on this side, and (iii) eventually substituting PEEK with sapphire.

To quantify, running such a setup for one hour with a quality factor $Q_0 = 3 \times 10^5$ at a frequency of 9 GHz and coupling $\beta = 2$ would reach an average value of $\approx 2 \times 10^{-14}$ GeV^{-1}, provided that the noise temperature is 0.5 K and the magnet is brought to 9 T. This value is a factor less than 1.5 from the benchmark KSVZ model.

ACKNOWLEDGMENTS

This work is supported by INFN (QUAX experiment), by the U.S. Department of Energy, Office of Science, National Quantum Information Science Research Centers, Superconducting Quantum Materials and Systems Center (SQMS) under Contract No. DE-AC02-07CH11359, by the European Union's FET Open SUPERGALAX project,

Grant No. 863313, and by the PNRR MUR Project No. PE0000023-NQSTI. This research was also supported by the Munich Institute for Astro-, Particle and BioPhysics (MIAPbP), which is funded by the Deutsche Forschungsgemeinschaft (DFG, German Research Foundation) under Germany's Excellence Strategy—EXC-2094–390783311. This paper is based upon work from COST Action COSMIC WISPers CA21106, supported by COST (European Cooperation in Science and Technology). The authors wish to acknowledge the technical support of Anna Calanca, Marco Beatrici, Stefano Lauciani, Maurizio Gatta, Giuseppe Pileggi, Giuseppe Papalino, and Daniele Di Bari, as well as of the Mechanical Workshop Department of the Mechanical Design and Construction Service (SPCM) of LNF, and Fabrizio Stivanello and Eduard Chyhyrynets from the National Laboratories of Legnaro for electropolishing the inner surface of the OFHC cavity.

APPENDIX

1. Dark photons

The dark photon (DP) is weakly coupled to ordinary fields through a small kinetic mixing χ with the visible photon [64]. We recast the limit on $g_{a\gamma\gamma}$ to one on χ considering the relation [64,65]:

$$\chi = g_{a\gamma\gamma}\frac{B}{m_{\mathrm{DP}}|\cos\theta|}, \tag{A1}$$

where B is the rms magnetic field value expressed in natural units, m_{DP} is the mass of the dark photon, and $\cos\theta = X \cdot B$. The vector X is the polarization of the dark photon field. Two different scenarios need to be evaluated. In a random polarization scenario, $\cos^2\theta$ always assumes the value $1/3$, while in a linear polarization scenario, the value of $\cos\theta$ is an average over the acquisition time. We limit our discussion to the random polarization scenario since for the second one, there is no consensus on which procedure should be used [64,65]. Figure 8 shows the limits on χ obtained applying Eq. (A1) to the data of Fig. 7, using $\cos\theta = 1/\sqrt{3}$.

2. Calibration procedure

To calibrate the output power, we need to know the gain of the readout line ($L5$). We follow the procedure developed in [66]. The rf diagram of Fig. 1 can be represented, in dB units, by the following system of three coupled equations:

$$\begin{aligned} S_{51} &= G_{L1} + S_{21}^{\mathrm{cav}}(\nu_c, Q_0, \beta) + G_{L5}, \\ S_{53} &= G_{L3} + S_{22}^{\mathrm{cav}}(\nu_c, Q_0, \beta) + G_{L5}, \\ S_{13} &= G_{L1} + S_{12}^{\mathrm{cav}}(\nu_c, Q_0, \beta) + G_{L3}, \end{aligned} \tag{A2}$$

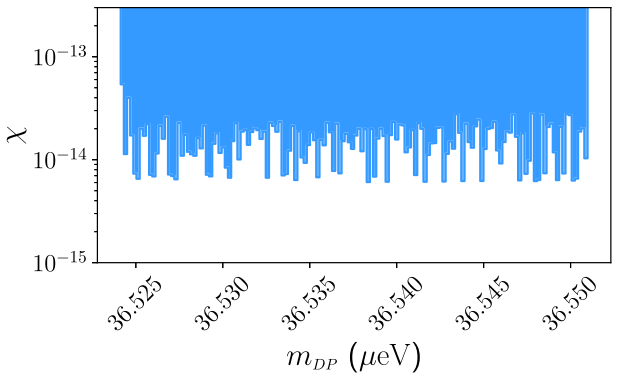

FIG. 8. The 90% single-sided CL upper limit for the kinetic mixing χ as a function of the DP mass, in the random polarisation scenario.

where S_{51}, S_{53}, and S_{13} are the measured scattering parameters, G_{L1}, G_{L3}, and G_{L5} are the attenuations/gains of the respective input and output lines, and S_{ij}^{cav} are the Lorentzian functions of the cavity:

$$S_{21}^{\mathrm{cav}} = S_{12}^{\mathrm{cav}} = 20\log_{10}\left|\frac{2\sqrt{\beta_1\beta_2}}{1+\beta_1+\beta_2+jQ_0\delta}\right|, \tag{A3}$$

$$\begin{aligned} S_{22}^{\mathrm{cav}} = 20\log_{10}\Bigg|&\frac{\beta_2^2-(1+\beta_1)^2-(Q_0\delta+q)^2}{(1+\beta_1+\beta_2)^2+Q_0^2\delta^2} \\ &- j\frac{2\beta_2 Q_0\delta}{(1+\beta_1+\beta_2)^2+Q_0^2\delta^2}\Bigg|, \end{aligned} \tag{A4}$$

where β_2 is the coupling to the mobile antenna, δ is equal to $\omega/\omega_0 - \omega_0/\omega$, and q is a parameter accounting for the small asymmetry in the reflection coefficient.

At each frequency step in Table I we perform a simultaneous fit of the S_{51}, S_{53} and S_{13} data. Note that in the fits, β_1 is kept fixed at 1.4×10^{-3}, the value expected from simulations, since it was verified to be less than 7×10^{-3} combining measurements of $L1$ and $L2$ data.

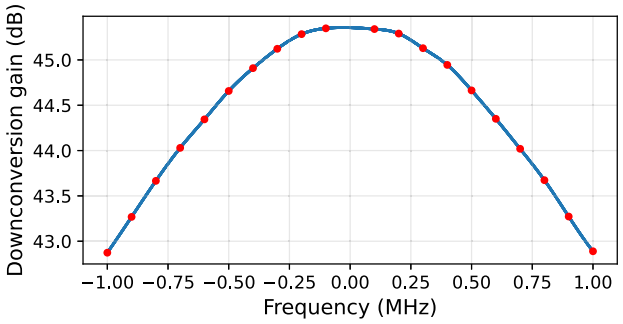

FIG. 9. Calibration of the downconversion electronics in the frequency band of the ADC.

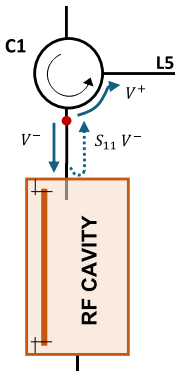

FIG. 10. Sketch of coherent sum of a frequency-dependent wave ($S_{11}V^-$) and a frequency-independent one (V^+), due to the emission of a non-thermalized point, shown in red.

Upon solving Eqs. (A2) using the parameters found from the fit, the gain of the readout line is

$$G_{L5} = \frac{(S_{51} - S_{21}^{\mathrm{cav}}) + (S_{53} - S_{22}^{\mathrm{cav}}) - (S_{13} - S_{12}^{\mathrm{cav}})}{2}, \qquad \text{(A5)}$$

evaluated as the average of the spectrum. The maximum spread of the G_{L5} values within all the subruns is only 0.4 dB so that we can reasonably consider the gain constant in the evaluated frequency range and equal to the average value of $G_{L5} = 70.62$ dB.

This value is referred at the input of the splitter. Since the S parameters are measured to and from the VNA ports, to calculate the right value for G_{L5}, the contributions of the splitter (−3 dB) and of the cable from the splitter to the VNA have been subtracted. Then, a calibration of the downconversion electronics from the splitter input to the DAQ is also necessary. This has been performed only once and is valid for all subruns since it does not depend on the frequency change. We send a known power at the splitter and measure the downconverted signal at the DAQ input with a spectrum analyzer, which gives an absolute power. We repeat the measurement at different LO frequencies to cover all the acquisition bandwidth of the ADC board, from −1 to 1 MHz. The calibration curve is shown in Fig. 9, where the roll-off is due to the ADC internal filters.

Finally, the downconversion calibration curve and the gain G_{L5} are subtracted to the raw power spectra acquired by the ADC to obtain calibrated power spectra (as the one in Fig. 5), where the power level is therefore referred at the cavity readout port.

3. Fano effects in power spectra

As indicated in Sec. III, we observe bump structures in the power spectra, showing typical interference features which we attribute to a series of combined effects. First, the bump is present due to a power excess with respect to a

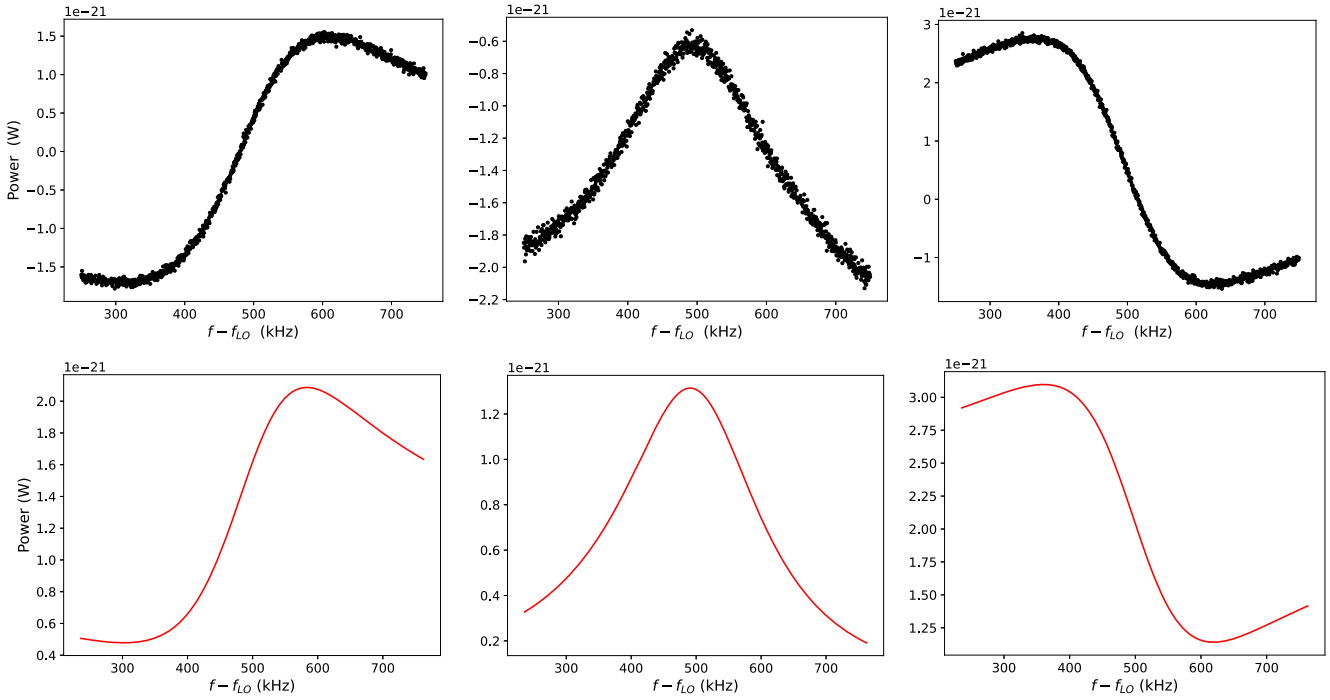

FIG. 11. Top: Experimental power spectra with central frequency of 8.8317690, 8.8341279 and 8.8377664 GHz. Here, the spectrum acquired with the antenna decoupled from the cavity has been subtracted. Bottom: Power spectra generated from Eq. (A6) at the same frequencies.

thermal background, in this case, caused by a thermal source inside the cavity with a temperature $T_{\rm cav} > T_{\rm base}$ (the "hot rod"). This would be symmetric (without Fano structures) if no other effect at the output port is present, but it is very likely that the circulator and/or the cable from the circulator to the cavity are not well thermalized at 20 mK. In fact, a fraction of the 4 K noise comes backward from the HEMT and from the attenuators (which are thermal emitters themselves); moreover, the cable is not anchored to the plate to be free to move as the piezo motor brings it down. Thus, the cable, circulator or connectors behave as a source of thermal background. Such a thermal source would emit in any direction (see the sketch of Fig. 10), and the wave V^+ toward the output line L5 would coherently sum with the wave V^- reflected by the cavity and redirected toward L5 as well.

To model the spectrum resulting from a frequency-dependent term and a background, we write the contributions similar to Eq. (1) of Ref. [57], resulting in

$$P = k_B T_{\rm circ} \Delta\nu |S_{11} e^{-i(\omega {\rm d}t+\varphi)} + 1|^2 + k_B T_{\rm cav} \Delta\nu |S_{21}|^2, \tag{A6}$$

where the last term is the thermal contribution from the cavity itself. Here, S_{11} and S_{21} are the standard scattering parameters. In Fig. 11, we compare qualitatively three spectra at frequencies of 8.8317690, 8.8341279, and 8.8377664 GHz, respectively, with the red curves generated with Eq. (A6), with reasonable values of $T_{\rm circ} = 0.45$ K, $T_{\rm cav} = 0.1$ K, ${\rm d}t = 10$ ns (electrical delay introduced by the cable), $\Delta\nu = 500$ Hz (bin width), $\varphi = -0.8$, -0.1, and 0.9.

A very thorough analysis with a fit procedure is not easily applicable since the parameters are very correlated, but the comparison gives a reasonable indication of the involved effective temperatures and parameters.

[1] S. Weinberg, Phys. Rev. Lett. **40**, 223 (1978).
[2] F. Wilczek, Phys. Rev. Lett. **40**, 279 (1978).
[3] R. D. Peccei and H. R. Quinn, Phys. Rev. Lett. **38**, 1440 (1977).
[4] R. D. Peccei and H. R. Quinn, Phys. Rev. D **16**, 1791 (1977).
[5] J. Preskill, M. B. Wise, and F. Wilczek, Phys. Lett. **120B**, 127 (1983).
[6] L. Abbott and P. Sikivie, Phys. Lett. **120B**, 133 (1983).
[7] M. Dine and W. Fischler, Phys. Lett. **120B**, 137 (1983).
[8] I. G. Irastorza and J. Redondo, Prog. Part. Nucl. Phys. **102**, 89 (2018).
[9] P. Sikivie, Phys. Rev. Lett. **51**, 1415 (1983).
[10] P. Sikivie, Phys. Rev. D **32**, 2988 (1985).
[11] N. Du *et al.*, Phys. Rev. Lett. **120**, 151301 (2018).
[12] C. Boutan *et al.*, Phys. Rev. Lett. **121**, 261302 (2018).
[13] T. Braine *et al.*, Phys. Rev. Lett. **124**, 101303 (2020).
[14] C. Bartram *et al.*, Phys. Rev. Lett. **127**, 261803 (2021).
[15] L. Zhong *et al.*, Phys. Rev. D **97**, 092001 (2018).
[16] K. Backes *et al.*, Nature (London) **590**, 238 (2021).
[17] M. J. Jewell *et al.* (HAYSTAC Collaboration), Phys. Rev. D **107**, 072007 (2023).
[18] B. T. McAllister, G. Flower, E. N. Ivanov, M. Goryachev, J. Bourhill, and M. E. Tobar, Phys. Dark Universe **18**, 67 (2017).
[19] A. Quiskamp, B. T. McAllister, P. Altin, E. N. Ivanov, M. Goryachev, and M. E. Tobar, Sci. Adv. **8**, eabq3765 (2022).
[20] S. Lee, S. Ahn, J. Choi, B. Ko, and Y. K. Semertzidis, Phys. Rev. Lett. **124**, 101802 (2020).
[21] J. Choi, S. Ahn, B. Ko, S. Lee, and Y. K. Semertzidis, Nucl. Instrum. Methods Phys. Res., Sect. A **1013**, 165667 (2021).
[22] J. Jeong, S. Youn, S. Bae, J. Kim, T. Seong, J. E. Kim, and Y. K. Semertzidis, Phys. Rev. Lett. **125**, 221302 (2020).
[23] O. Kwon *et al.*, Phys. Rev. Lett. **126**, 191802 (2021).
[24] Y. Lee, B. Yang, H. Yoon, M. Ahn, H. Park, B. Min, D. Kim, and J. Yoo, Phys. Rev. Lett. **128**, 241805 (2022).
[25] C. M. Adair *et al.*, Nat. Commun. **13** (2022).
[26] A. K. Yi *et al.*, Phys. Rev. Lett. **130**, 071002 (2023).
[27] T. Grenet, R. Ballou, Q. Basto, K. Martineau, P. Perrier, P. Pugnat, J. Quevillon, N. Roch, and C. Smith, arXiv: 2110.14406.
[28] A. Álvarez Melcón *et al.*, J. Cosmol. Astropart. Phys. 05 (2018) 040.
[29] A. Álvarez Melcón *et al.*, J. High Energy Phys. 07 (2020) 084.
[30] A. Álvarez Melcón *et al.*, J. High Energy Phys. 10 (2021) 075.
[31] H. Chang *et al.* (TASEH Collaboration), Phys. Rev. Lett. **129**, 111802 (2022).
[32] R. Barbieri, C. Braggio, G. Carugno, C. S. Gallo, A. Lombardi, A. Ortolan, R. Pengo, G. Ruoso, and C. C. Speake, Phys. Dark Universe **15**, 135 (2017).
[33] N. Crescini *et al.*, Eur. Phys. J. C **78**, 703 (2018).
[34] D. Alesini *et al.*, Phys. Rev. D **99**, 101101 (2019).
[35] N. Crescini *et al.*, Phys. Rev. Lett. **124**, 171801 (2020).
[36] D. Alesini *et al.*, Phys. Rev. D **103**, 102004 (2021).
[37] D. Alesini *et al.*, Phys. Rev. D **106**, 052007 (2022).
[38] R. Di Vora *et al.* (QUAX Collaboration), Phys. Rev. D **108**, 062005 (2023).
[39] D. Alesini *et al.*, Phys. Dark Universe **42**, 101370 (2023).
[40] S. Ahyoune *et al.*, Ann. Phys. (Berlin) **535**, 2300326 (2023).
[41] J. L. Ouellet *et al.*, Phys. Rev. Lett. **122**, 121802 (2019).
[42] L. Brouwer *et al.* (DMRadio Collaboration), Phys. Rev. D **106**, 103008 (2022).
[43] L. Brouwer *et al.* (DMRadio Collaboration), Phys. Rev. D **106**, 112003 (2022).
[44] B. Aja *et al.*, J. Cosmol. Astropart. Phys. 11 (2022) 044.

[45] A. Caldwell, G. Dvali, B. Majorovits, A. Millar, G. Raffelt, J. Redondo, O. Reimann, F. Simon, and F. Steffen, Phys. Rev. Lett. **118**, 091801 (2017).
[46] M. Lawson, A. J. Millar, M. Pancaldi, E. Vitagliano, and F. Wilczek, Phys. Rev. Lett. **123**, 141802 (2019).
[47] Z. Zhang, D. Horns, and O. Ghosh, Phys. Rev. D **106**, 023003 (2022).
[48] J. F. Hernández-Cabrera *et al.*, Symmetry **16**, 163 (2024).
[49] F. Bajjali *et al.*, J. Cosmol. Astropart. Phys. 08 (2023) 077.
[50] J. Liu *et al.* (BREAD Collaboration), Phys. Rev. Lett. **128**, 131801 (2022).
[51] K. Schmieden and M. Schott, *Proc. Sci.*, EPS-HEP2021 (2021) 141.
[52] B. M. Brubaker *et al.*, Phys. Rev. Lett. **118**, 061302 (2017).
[53] D. Kim, J. Jeong, S. Youn, Y. Kim, and Y. K. Semertzidis, J. Cosmol. Astropart. Phys. 03 (2020) 066.
[54] P. A. Zyla *et al.* (Particle Data Group), Prog. Theor. Exp. Phys. **2020**, 083C01 (2020).
[55] M. S. Turner, Phys. Rev. D **42**, 3572 (1990).
[56] ANSYS HFSS software, https://www.ansys.com/products/electronics/ansys-hfss.
[57] D. Rieger, S. Günzler, M. Spiecker, A. Nambisan, W. Wernsdorfer, and I. Pop, Phys. Rev. Appl. **20**, 014059 (2023).
[58] A. Savitzky and M. J. Golay, Anal. Chem. **36**, 1627 (1964).
[59] R. H. Dicke, in *Classics in Radio Astronomy* (Springer, Dordrecht, 1946), pp. 106–113, 10.1007/978-94-009-7752-5_11.
[60] G. Cowan, K. Cranmer, E. Gross, and O. Vitells, arXiv:1105.3166.
[61] J. E. Kim, Phys. Rev. Lett. **43**, 103 (1979).
[62] M. Shifman, A. Vainshtein, and V. Zakharov, Nucl. Phys. **B166**, 493 (1980).
[63] C. O'Hare, cajohare/axionlimits: Axionlimits, https://cajohare.github.io/AxionLimits/ (2020).
[64] A. Caputo, A. J. Millar, C. A. O'Hare, and E. Vitagliano, Phys. Rev. D **104**, 095029 (2021).
[65] P. Arias, D. Cadamuro, M. Goodsell, J. Jaeckel, J. Redondo, and A. Ringwald, J. Cosmol. Astropart. Phys. 06 (2012) 013.
[66] C. Braggio *et al.*, Rev. Sci. Instrum. **93**, 094701 (2022).